Rare Metal Materials and Engineering
Volume 51, Issue 5, May 2022
Available online at www.rmme.ac.cn

Science Press

Cite this article as: Zhu Pengfei, Wang Qian, Wu Chaoling, et al. Effect of Nitrogen and Oxygen Impurities on Chemical Composition, Microstructure, and Hydrogen Storage Performance of $V_{40}Ti_{26}Cr_{26}Fe_8$ Alloy[J]. Rare Metal Materials and Engineering, 2022, 51(05): 1582-1588.

ARTICLE

Effect of Nitrogen and Oxygen Impurities on Chemical Composition, Microstructure, and Hydrogen Storage Performance of $V_{40}Ti_{26}Cr_{26}Fe_8$ Alloy

Zhu Pengfei[1], Wang Qian[1], Wu Chaoling[1,3], Chen Yungui[2,3], Yan Yigang[2,3], Wang Yao[2,3]

[1] College of Materials Science and Engineering, Sichuan University, Chengdu 610064, China; [2] Institute of New-Energy and Low-Carbon Technology, Sichuan University, Chengdu 610065, China; [3] Engineering Research Center of Alternative Energy Materials & Devices, Ministry of Education, Chengdu 610064, China

Abstract: The synergetic effects of nitrogen and oxygen impurities on the micro-area chemical composition, microstructure, and hydrogen storage performance of V-Ti-Cr-Fe alloys were investigated through X-ray diffraction, scanning electron microscopy, optical microscopy, and pressure-composition-temperature (PCT) analyses. Results show that the hydrogen storage capacity of $V_{40}Ti_{26}Cr_{26}Fe_8$ alloy is obviously decreased with increasing the nitrogen and oxygen impurities. The mechanism for the decrease is as follows: the oxygen dissolved in V-based alloys suppresses the formation of the dihydride phase, resulting in the decrease in hydrogen capacity (primary effect); while the nitrogen is bound with titanium forming a new nitrogen-titanium-enriched phase, which results in composition change of the main phase and decreases the lattice parameter (secondary effect).

Key words: V-Ti-Cr-Fe alloy; hydrogen storage performance; nitrogen and oxygen impurities; lattice parameter

Hydrogen is a suitable and environmental-friendly energy storage medium because of its easy availability and eco-friendliness of non-polluting products after combustion[1]. The efficient storage of hydrogen is one of the key technical problems in the hydrogen energy field. Compared with the high-pressure gaseous hydrogen storage and cryogenic liquid hydrogen storage, the solid hydrogen storage method has the merits of high volumetric hydrogen storage density and high safety[2].

The vanadium-based alloy has a high hydrogen storage capacity of around 3.8wt% in theory and excellent hydrogenation-dehydrogenation kinetics under moderate temperature and pressure conditions[3]. Many studies have been conducted to improve the hydrogen storage performance of V-based materials. The application of ferro-vanadium alloy greatly reduces the production cost of the V-based alloy and the iron has few adverse effects on hydrogen storage capacity, thereby building a foundation for the industrialized production of V-based hydrogen storage materials[4,5]. The heat treatment can eliminate some defects in the as-cast alloys, result in lower thermal stability of the hydride, and improve the activation performance and kinetic properties[6]. Luo et al[7] showed that the smaller the particle size of V-based alloy in the range of 38~250 μm, the lower the micro-strain in the lattice owing to the easier micro-stress release, and thus the better the hydrogen absorption-desorption cycle performance. The addition of alloying element can modify the interactions between the specimen and hydrogen, which drastically improves the hydrogen absorption characteristics[8-17]. Yan et al[18,19] found that Al and Si impurities in raw materials have great influences on hydrogen storage properties of V-based alloy. The effects of oxygen on microstructure and hydrogen storage performance for V-based alloy were reported in Ref.[20-22]. However, most reports only focus on the oxygen impurity, ignoring the possible changes in the microstructure and chemical composition in the micro-area of alloys when other impurities are introduced in process.

The effects of nitrogen impurities on the microstructure and

Received date: May 15, 2021
Foundation item: International/Hongkong, Macao & Taiwan Scientific and Technological Innovation Cooperation Project (2019YFH0148)
Corresponding author: Wu Chaoling, Ph. D., Professor, College of Materials Science and Engineering, Sichuan University, Chengdu 610064, P. R. China, E-mail: wuchaoling@scu.edu.cn

properties of V-based hydrogen storage alloys are rarely reported. The nitrogen and oxygen impurities are possibly introduced in the high-temperature process of arc melting and/or heat treatment. In this research, the synergistic effects of nitrogen and oxygen impurities on the chemical composition, microstructure, and hydrogen storage performance of V-based alloys were investigated.

1 Experiment

Three ingots of $V_{40}Ti_{26}Cr_{26}Fe_8$ alloy were named as specimen A, specimen B, and specimen C and were prepared by arc melting under argon-oxygen-nitrogen mixtures in different proportions in the ferro-vanadium materials. The content of Ti and Cr purities was 99.8wt% and 99.8wt%, respectively. The nitrogen and oxygen contents of the three alloys were analyzed by the inert gas fusion-infrared radiation (IR) method (TCH-600, LECO). The difference in oxygen and nitrogen contents is listed in Table 1.

The specimen A had a little nitrogen and oxygen, specimen B contained the moderate content of nitrogen and oxygen, and specimen C was rich in nitrogen and oxygen. Each alloy was turned over and remelted at least four times to ensure the homogeneity of chemical composition, and then annealed at 1623 K for 30 min under vacuum condition in ZM-16 vacuum molybdenum wire furnace followed by furnace cooling to room temperature.

The crystal structures of the alloys were analyzed by X-ray diffractometer (XRD, DX-2700B) with an operating voltage of 40 kV and current of 30 mA. The structure refinement was conducted by marching step scanning under the conditions of scanning speed of 0.05°/s, sampling time of 2 s, and scanning angle of 30°~90°. The structure and morphology were observed using an optical microscope (OM, JX-2000B). The alloys were ground successively with various sandpaper and polished with metallographic polishing paste. The well-polished surfaces were further corroded by a corrosive agent of 10vol% HF+20vol% HNO_3+70vol% H_2O, then rinsed with deionized water, cleaned with alcohol, and finally blow-dried. The alloy microtopography and micro-area chemical composition were analyzed by scanning electron microscope (SEM, U-8200) equipped with energy dispersive spectrometer (EDS, Oxford X-Max). Furthermore, the composition of main and secondary phases was determined by EDS.

The Sieverts-type device was applied to study the hydrogen absorption-desorption properties of the alloys at 298 K under the cut-off pressure of 0.001 MPa. Firstly, all alloys were broken into small pieces of 1~4 mm in size and then put into a stainless-steel reactor for initial hydrogen absorption kinetics and pressure-composition-temperature (PCT) tests. The reactor containing alloy pieces was vacuumized at 673 K for 30 min, and then slowly cooled down to room temperature. The hydrogen (99.999wt%) with 4 MPa pressure was introduced into the reactor and the molar amount of hydrogen participating in the reaction was accurately calculated through the data from pressure gauge.

Table 1 Nitrogen and oxygen contents of specimen A, specimen B, and specimen C (wt%)

Specimen	N	O
A	0.024	0.045
B	0.202	0.078
C	0.264	0.170

2 Results and Discussion

2.1 Microstructure and micro-area chemical composition analysis

The microstructures of the $V_{40}Ti_{26}Cr_{26}Fe_8$ alloys with different contents of N and O impurities are shown in Fig. 1. The three alloys are all composed of two phases: the gray main phase and the black secondary phase. In addition, the amount of the secondary phase is increased with increasing the N and O impurities. EDS results of different phases in specimens are listed in Table 2 to demonstrate the detailed composition. It is clear that Ti content in the secondary phase is significantly higher than in the main phase, suggesting that a titanium-rich phase is generated. The nitrogen is almost completely enriched in the secondary phase, and its content is significantly increased with increasing the N and O impurities. Meanwhile, the oxygen is dispersed throughout specimens without significant content difference in the main and secondary phases, whereas its content is increased with increasing the N and O impurities, which is consistent with results in Table 1.

Fig. 2 shows the morphologies of the enriched secondary

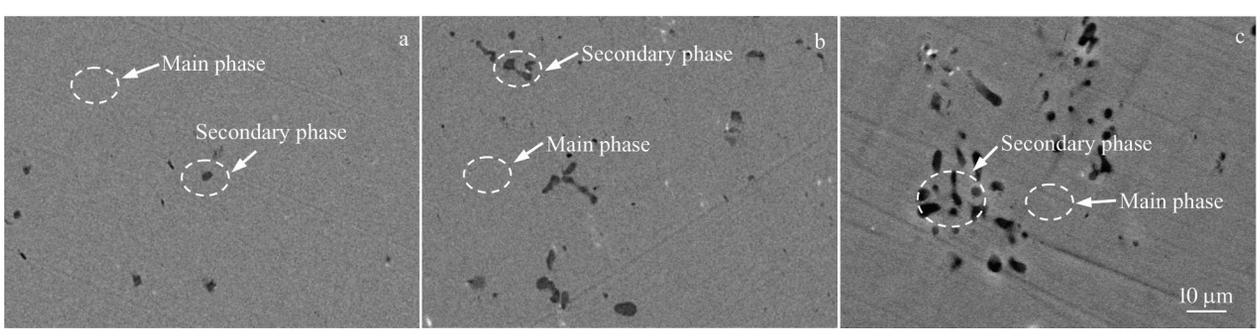

Fig.1 SEM microstructures of $V_{40}Ti_{26}Cr_{26}Fe_8$ alloys of specimen A (a), specimen B (b), and specimen C (c)

Table 2 EDS results of chemical composition of different phases in $V_{40}Ti_{26}Cr_{26}Fe_8$ alloy specimens (wt%)

Specimen	Phase	V	Ti	Cr	Fe	N	O
A	Main phase	40.08	25.70	24.78	7.37	0	2.05
	Secondary phase	24.27	53.83	13.28	3.84	1.57	3.21
B	Main phase	38.90	24.87	24.97	7.40	0	3.87
	Secondary phase	18.45	55.26	12.33	2.66	6.67	4.81
C	Main phase	38.01	23.89	24.76	7.37	0	6.13
	Secondary phase	14.21	60.17	8.28	2.33	8.51	6.32

phase in specimen C. The nitrogen is enriched in the secondary phase, while oxygen is dissolved throughout in the V-based alloys without prominent compositional fluctuation.

2.2 Metallographic structure analysis

The observed grain morphology is simplified as a cuboid with specific length, width, and height, as shown in Fig.3. The metallographic microstructures in longitudinal section and cross section of specimen A, specimen B, and specimen C are shown in Fig. 4. The specimen A is composed of columnar grains, specimen C is composed of equiaxed grains, and specimen B has the mixture structure of columnar grains and equiaxed grains. The average grain sizes of hypothetical grain in different specimens are shown in Table 3. The width and height are almost the same while the length (L) is quite different among different specimens with L_A:L_B:L_C=8:4:1 (L_A, L_B, and L_C represent the grain length on the longitudinal section of specimen A, specimen B and specimen C, respectively). The crystal growth in specimen A has obvious directionality, while that in specimen C has no directionality, and that in specimen B shows a relatively weak directionality. Therefore, the impurities play a role in grain size regulation: the less the nitrogen and oxygen in alloy, the larger the grains.

From the perspective of thermodynamics, the homogeneous nucleation is spontaneous due to the supercooling, even in the liquid. In fact, the metal inevitably contains some refractory impurities which are distributed in the liquid in the melting process. The impurities provide a favorable surface for the generation of crystal nucleuses in the liquid and reduce the interface energy. This process is heterogeneous nucleation, which can be expressed by Eq.(1), as follows:

$$\Delta W_{he}^{*}=\frac{16}{3}\frac{\pi\sigma_{Lc}^{3}T_{m}^{2}}{3L^{2}(\Delta T)^{2}}\left[\frac{2-3\cos\theta+\cos\theta^{3}}{4}\right]=\Delta W_{ho}^{*}f(\theta) \quad (1)$$

where ΔW_{he}^{*} is heterogeneous nucleation work, ΔW_{ho}^{*} is homogeneous nucleation work, σ_{Lc} is the unit interface free energy between the liquid phase and the crystal nucleus, T_m is the melting point of the metal, L is the absorbed latent heat of fusion during the transition from solid phase to liquid phase, ΔT is the undercooling degree, and $f(\theta)$ is a function of θ angle with $0°<\theta<180°$. As $0°<\theta<180°$ and $-1<\cos\theta<1$, $f(\theta)$ changes within the range of $-1<f(\theta)<1$, as shown in Eq.(2):

$$f(\theta)=\frac{2-3\cos\theta+\cos\theta^{3}}{4} \quad (2)$$

So the heterogeneous nucleation work is less than the homogeneous nucleation work. The refractory impurities distributed in the liquid create favorable conditions for the generation of crystal nucleuses during the process of heterogeneous nucleation on the surface of these impurities, as shown in Fig. 5. The nitrogen impurity introduced in processing is bound with titanium to form nitrogen-titanium-enriched secondary phase, which has a much higher melting point than other substances in the melting process. During the cooling and crystallization, the secondary phase acts as a heterogeneous crystal nucleus to promote the V-based alloy nucleation. The nitrogen-titanium-enriched secondary phase is distributed uniformly in the V-based alloy liquid as a grain refiner, as shown in Fig.6. Thus, the more the impurities in the

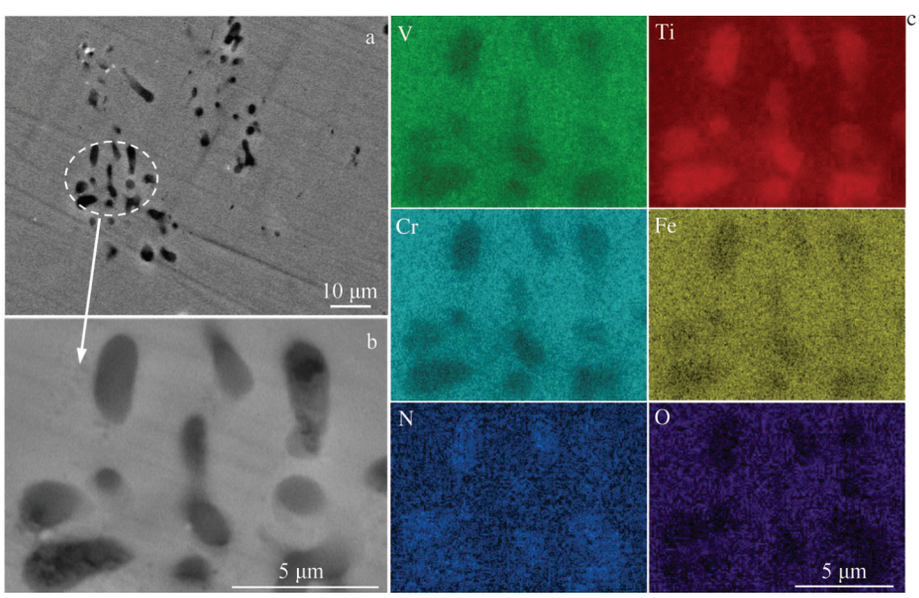

Fig.2 SEM image of enriched secondary phase in specimen C (a); SEM image of magnified circle area in Fig.2a (b) and corresponding element distributions of V, Ti, Cr, Fe, N, O for secondary phase (c)

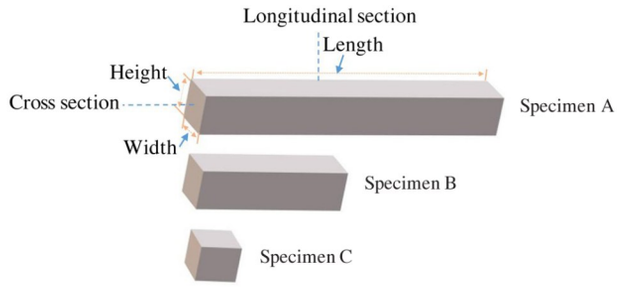

Fig.3 Schematic diagram of grain morphologies with specific length, width, and height of specimen A, B, and C

alloy solution, the more the favorable sites for nucleation and the smaller the crystal grains.

2.3 Crystal structure of alloy before and after hydrogenation

XRD analysis was applied to investigate the evolution of crystal structure during the whole process of hydrogen storage and release. The XRD patterns of the three alloys before hydrogen absorption are shown in Fig. 7a. Although the metallographic structures of different specimens are quite different, XRD patterns of all the specimens are similar, indicating that they are all composed of the single V-based body-centered cubic (bcc) phase, namely the hydrogen absorbing phase. The content of the secondary phase in nitrogen and titanium of the three specimens is too insufficient to be detected by XRD. Therefore, the Rietveld refinement method is used, as shown in Fig. 8. The detailed lattice parameters of the main bcc phase of specimen A, B, and C are 0.3036, 0.3023, and 0.3015 nm, respectively, as shown in Table 4. The lattice parameter is decreasesd with increasing the impurity content, because the content of Ti which has a larger atomic size than V, Fe, and Cr is decreased in the main phase due to the formation of nitrogen-titanium-enriched phase, which is consistent with the results in Ref.[23].

The hydrogen absorption kinetics experiments were conducted firstly, and then XRD analysis was performed on the powders after hydrogenation, as shown in Fig. 7b. The crystal structures of the three specimens after hydrogen absorption are quite different. Specimen A and B after hydrogenation are composed of two phases: VH_2 and $V_4H_{2.88}$. The diffraction peak intensity of VH_2 phase of specimen B is weaker than that of specimen A, which demonstrates that less VH_2 phase is generated in specimen B. Specimen C mainly consists of $V_4H_{2.88}$ phase. The contents of VH_2 phase in specimen A, B, and C calculated by Rietveld refinement method are 33.3wt%, 13.4wt%, and 0.6wt%, respectively, as shown in Table 5. The content of VH_2 phase is decreased with increasing the impurity content. It is reported that the oxygen dissolved in V-based alloy suppresses the formation of the dihydride[22]. Thus, it can be deduced that oxygen is one of the critical factors to reduce the hydrogen storage capacity of the alloy.

All dehydrogenated specimens only contain the single $V_4H_{2.88}$ phase, as shown in Fig.7c. It is concluded that the VH_2 phase disappears during the dehydrogenation process, but $V_4H_{2.88}$ remains. This is because the dihydride phase is unstable and easily decomposes under the moderate temperature and pressure, while the $V_4H_{2.88}$ phase is thermally stable, which requires much higher temperature for dehydrogenation[4].

2.4 Performance of hydrogen absorption and desorption

The hydrogen absorption kinetic curve is usually used to study the hydrogen absorption ability. As shown in Fig. 9, at 298 K, the specimen A has an excellent hydrogen absorption kinetic with a maximum hydrogen absorption capacity of

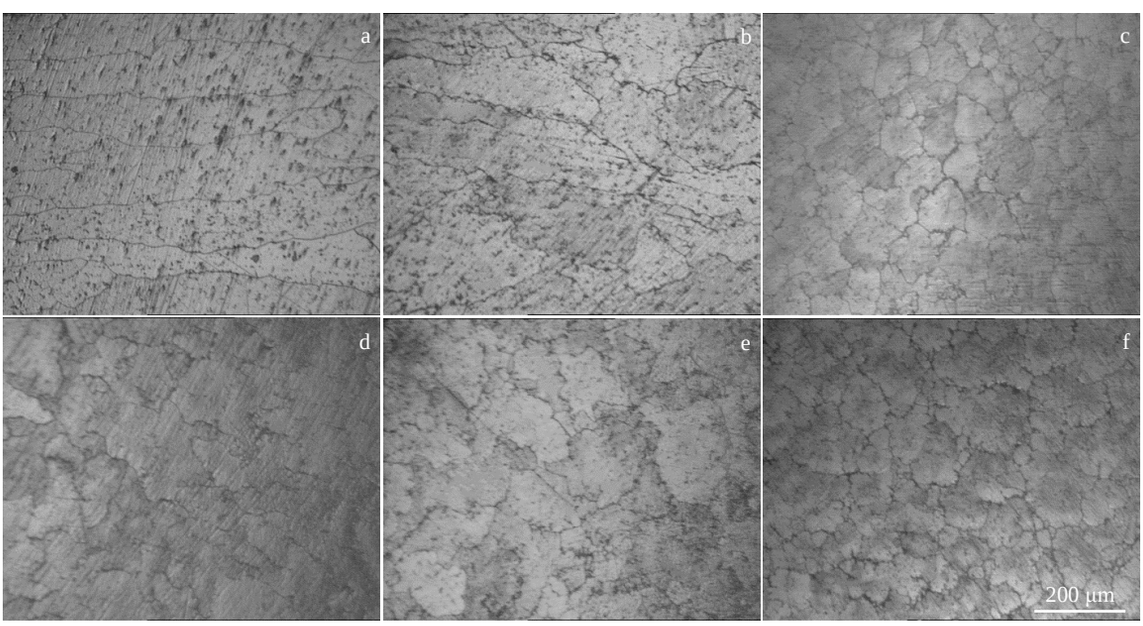

Fig.4 OM images of longitudinal sections (a~c) and cross sections (d~f) of microstructures in specimen A (a, d), specimen B (b, e) and specimen C (c, f)

Table 3 Average grain sizes of hypothetical grains in specimen A, B, and C (μm)

Specimen	Length	Width	Height
A	900	141	101
B	469	142	134
C	110	142	115

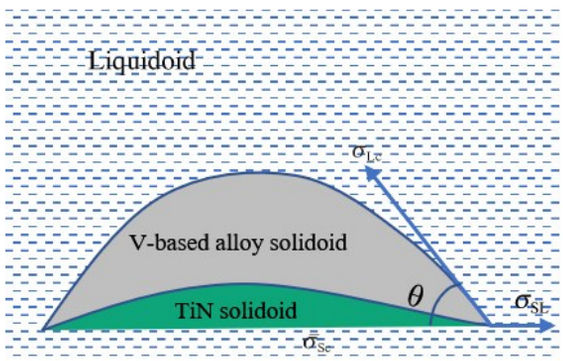

Fig.5 Schematic diagram of heterogeneous nucleation in V-based alloy

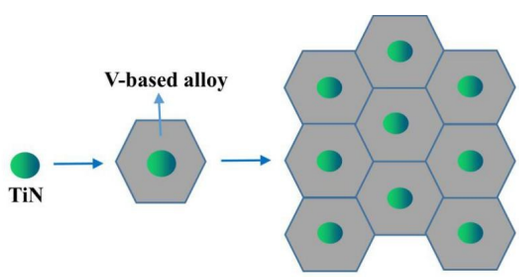

Fig.6 Schematic diagram of nitrogen-titanium-enriched phase as grain refiner in V-based alloy

3.94wt% in 40 min. The rapid adsorption occurs in the first 5 min, and 79% of the maximum amount of hydrogen is absorbed. However, the specimen B only absorbs maximally 2.03wt% hydrogen, and specimen C has the lowest hydrogen absorption capacity of only 1.58wt% in the same duration. The PCT curves of the hydrogen release are shown in Fig.10. The specimen A has the largest hydrogen desorption capacity of 2.1wt% with a wide and flat equilibrium plateau pressure, while specimen B and specimen C have desorption capacities of 0.6wt% and 0.3wt%, respectively, with narrow and tilted plateau pressures.

The hydrogen storage performance of V-based alloy depends strongly on the impurity content. As the nitrogen and oxygen impurities are introduced together, two possible effects should be taken into consideration. The effect of interstitial nitrogen on hydrogen storage performance in vanadium-based alloys was investigated in Ref.[23]. When the N content is 0.4wt%, the maximum hydrogen content is slightly decreased by approximately 6%, compared with that of pure V material. Yamanaka et al[24] found that adding 0.7wt% nitrogen in the $V_{0.37}Ti_{0.33}Mn_{0.30}$ alloy results in a slight decrease in maximum hydrogen content by about 5% at the first cycle. In this research, the content of nitrogen is less than 0.3wt%. A small amount of nitrogen is accumulated in the secondary phase, and the majority of nitrogen is mainly bound with titanium, which causes the composition change of the main phase and therefore reduces the lattice parameter. It is inferred that the dissolved nitrogen has an negligible effect on the maximum hydrogen storage capacity, i.e., the dissolved nitrogen has the secondary effect on the hydrogen absorption properties of V-based alloys. It is reported that even a small amount of oxygen can deteriorate the hydrogen storage capacity of V-based alloy[20-22]. Ref.[25] reports that the oxygen atoms are on the octahedral interstice in bcc lattice. The normal hydrogen absorption sites are decreased as the oxygen atoms occupy the interstitial sites. Furthermore, the hydrogen diffusion is suppressed strongly as a result of direct interaction between oxygen and hydrogen. The formation of the dihydride phase is hindered by the dissolved oxygen and its content is decreased with increasing the oxygen impurities, which is the primary effect of impurity content on the hydrogen absorption properties. Asano et al[22] explained the inhibiting effect from the perspective of binding energy of the O-H pair. Thus, the dissolved oxygen has a significant effect on the hydrogen storage capacity of V-based alloy.

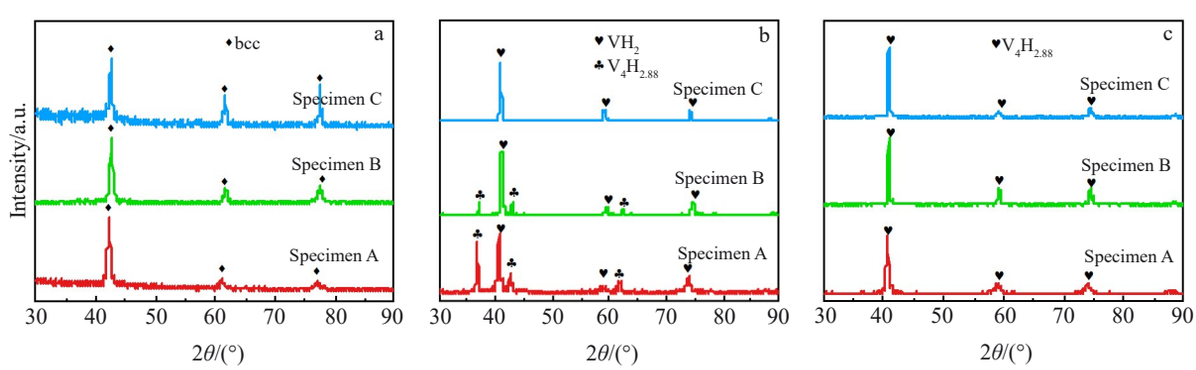

Fig.7 XRD patterns of specimen A, B, and C before hydrogenation (a), after hydrogenation (b), and after dehydrogenation (c)

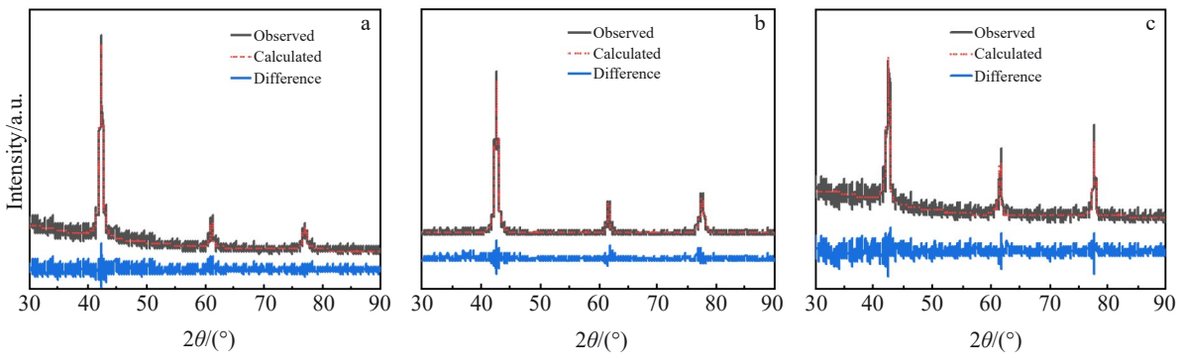

Fig.8 XRD patterns by Rietveld refinement of specimen A (a), specimen B (b), and specimen C (c) before hydrogenation

Table 4 Lattice parameters of main bcc phase in $V_{40}Ti_{26}Cr_{26}Fe_8$ alloy specimens before hydrogenation (nm)

Specimen	Lattice parameter
A	0.3036
B	0.3023
C	0.3015

Table 5 Hydride phase contents of $V_{40}Ti_{26}Cr_{26}Fe_8$ specimens after hydrogenation (wt%)

Specimen	VH_2	$V_4H_{2.88}$
A	33.3	66.7
B	13.4	86.6
C	0.6	99.4

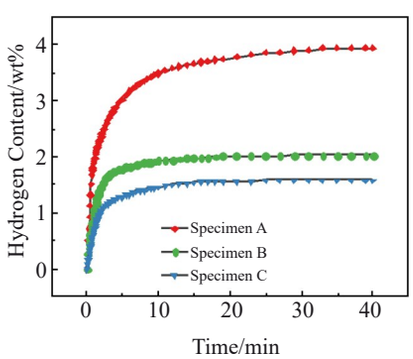

Fig.9 Hydrogen absorption kinetic curves of $V_{40}Ti_{26}Cr_{26}Fe_8$ alloy specimens at 298 K

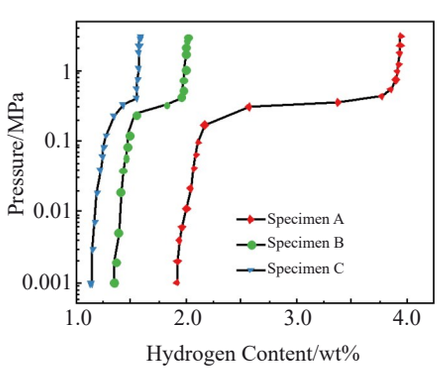

Fig.10 PCT curves of hydrogen release of $V_{40}Ti_{26}Cr_{26}Fe_8$ alloy specimens at 298 K

3 Conclusions

1) The hydrogen absorption/desorption capacity of $V_{40}Ti_{26}Cr_{26}Fe_8$ alloys is decreased sharply with increasing the nitrogen and oxygen impurities introduced during the manufacturing process. At 298 K, the alloy with less nitrogen and oxygen has excellent hydrogenation-dehydrogenation kinetics with a maximum hydrogen absorption capacity of 3.94wt% and desorption capacity of 2.1wt%. While the alloy with a relatively large amount of nitrogen and oxygen only has a maximum hydrogen absorption capacity of 1.58wt% and desorption capacity of 0.3wt%.

2) The primary effect mechanism of nitrogen and oxygen contents on the hydrogenation properties is that the oxygen dissolved in the V-based alloys hinders the normal hydrogen occupation and suppresses the formation of the dihydride phase, resulting in the decrease in the hydrogen capacity. The formation of the nitrogen-titanium-enriched secondary phase induces a composition change of the main phase, resulting in the decrease in lattice parameter, which is the secondary effect.

3) The nitrogen-titanium-enriched secondary phase acts as a heterogeneous crystal nucleus during the cooling and crystallization process, and promotes the nucleation of the $V_{40}Ti_{26}Cr_{26}Fe_8$ alloy. The secondary phase reduces the grain size of alloys as a grain refiner.

References

1 Schlapbach L, Züttel A. *Nature*[J], 2001, 414(6861): 353

2 Sakintuna B, Lamari-Darkrim F, Hirscher M. *International Journal of Hydrogen Energy*[J], 2007, 32(9): 1121

3 Yan Y G, Chen Y G, Liang H *et al*. *Journal of Alloys & Compounds*[J], 2006, 454(1-2): 427

4 Kumar S, Jain A, Ichikawa T *et al*. *Renewable & Sustainable Energy*[J], 2017, 72: 791

5 Yan Y G, Chen Y G, Wu C L *et al*. *Journal of Power Sources*[J], 2007, 164(2): 799

6 Zhou H Y, Wang F, Wang J *et al*. *International Journal of Hydrogen Energy*[J], 2014, 39(27): 14 887

7 Luo L S, Wu C L, Yang S *et al*. *Journal of Alloys & Compounds* [J], 2015, 645(S1): 178

8 Bibienne T, Razafindramanana V, Bobet J L *et al*. *Journal of*

Alloys & Compounds[J], 2015, 620: 101
9 Chen Z G, Luo L S, Su Z J *et al*. *International Journal of Hydrogen Energy*[J], 2019, 44(26): 13 538
10 Kamble A, Sharma P, Huot J. *International Journal of Hydrogen Energy*[J], 2017, 42(16): 11 523
11 Kumar A, Banerjee S, Bharadwaj S R *et al*. *Journal of Alloys & Compounds*[J], 2015, 649: 801
12 Kumar S, Tiwari G P, Krishnamurthy N. *Journal of Alloys & Compounds*[J], 2015, 645: 252
13 Balcerzak M, Wagstaffe M, Robles R *et al*. *International Journal of Hydrogen Energy*[J], 2020, 45(53): 28 996
14 Mgs A, Avda B, Nes C *et al*. *International Journal of Hydrogen Energy*[J], 2020, 45(14): 7929
15 Jin Hangjun, Zhang Jinlong, Meng Xianghai *et al*. *Rare Metal Materials and Engineering*[J], 2008, 37(5): 803 (in Chinese)
16 Chen Lixin, Liu Jian, Xiao You *et al*. *Rare Metal Materials & Engineering*[J], 2005, 34(5): 705 (in Chinese)
17 Chen Lixin, Liu Jian, Wang Xinhua *et al*. *Rare Metal Materials & Engineering*[J], 2006, 35(5): 682
18 Yan Y G, Chen Y G, Hao L *et al*. *Journal of Alloys & Compounds*[J], 2007, 441(1-2): 297
19 Yan Y G, Chen Y G, Hao L *et al*. *Journal of Alloys & Compounds*[J], 2006, 426(1-2): 253
20 Tsukahara M, Takahashi K, Isomura A *et al*. *Journal of Alloys & Compounds*[J], 1998, 265(1-2): 257
21 Ulmer U, Asano K, Bergfeldt T *et al*. *International Journal of Hydrogen Energy*[J], 2014, 39(35): 20 000
22 Asano K, Hayashi S, Mimura K *et al*. *Acta Materialia*[J], 2016, 103: 23
23 Sakaki K, Kim H, Iwase K *et al*. *Journal of Alloys & Compounds* [J], 2018, 750: 33
24 Yamanaka S, Kashiwara Y, Sugiyama H *et al*. *Journal of Nuclear Materials*[J], 1997, 247: 244
25 Kim H, Sakaki K, Nakamura Y. *Materials Transactions*[J], 2014, 55(8): 1144

氮、氧杂质对$V_{40}Ti_{26}Cr_{26}Fe_8$合金化学成分、微观组织和贮氢性能的影响

朱鹏飞[1]，王　倩[1]，吴朝玲[1,3]，陈云贵[2,3]，严义刚[2,3]，王　尧[2,3]
(1. 四川大学 材料科学与工程学院，四川 成都 610064)
(2. 四川大学 新能源与低碳技术研究院，四川 成都 610065)
(3. 后续能源材料与器件教育部工程研究中心，四川 成都 610064)

摘　要：采用X射线衍射、扫描电子显微镜、光学显微镜和压力-成分-温度（PCT）等手段研究了氮、氧杂质对V-Ti-Cr-Fe合金微区化学成分、微观结构和贮氢能力的协同影响。$V_{40}Ti_{26}Cr_{26}Fe_8$合金的贮氢能力随着氮、氧杂质含量的增加而明显降低，主要作用机理如下：氧在V基合金中的溶解抑制了二氢化物相的形成，导致氢容量的降低（主要效应），而氮与钛结合形成了新的富氮钛相，导致了主相成分的变化和晶格参数的减小（二次效应）。

关键词：V-Ti-Cr-Fe合金；贮氢性能；氮氧杂质；晶格常数

作者简介：朱鹏飞，男，1995年生，硕士生，四川大学材料科学与工程学院，四川 成都 610064，E-mail：1303488299@qq.com